machines

MDPI

Article

Comprehensive Analysis of the Output Characteristics of Flow Field in Turbodrill Motor

Wei Li [1,2,3], Fulu Chen [1,2,*], Mengyu Cao [4], Tianchi Ma [1], Wangluo Ning [1], Mingxiu Zhang [1], Tiansu He [1] and Xu Wang [1]

[1] Institute of Petroleum Engineering, Northeast Petroleum University, Daqing 163318, China
[2] Key Laboratory for Enhanced Oil & Gas Recovery, Ministry of Education, Daqing 163318, China
[3] National Engineering Research Center of Oil & Gas Drilling and Completion Technology, Beijing 102206, China
[4] School of Mechanical Science and Engineering, Northeast Petroleum University, Daqing 163318, China
* Correspondence: cfleducation@163.com

Abstract: Turbodrills are extensively utilized within the oilfield development industry. In order to enhance the performance output of turbodrills, a novel stator and rotor structure has been conceptualized. Fluent 19.0 numerical simulation software was employed to ascertain the output characteristics of the rotor within the flow field. The drilling engine output performance was the subject of a qualitative study, which was conducted using the drilling mud pump test equipment during drilling. Furthermore, a speed torque meter measurement system was designed to quantitatively analyze the output torque and speed performance of the prototype. The results show that: ① Through the numerical simulation method, it is verified that the new structural rotor has the output performance of a conventional rotor. ② Comparing the numerical solution and the test value, it can be seen that the relative error value is within 4.3%, indicating that the numerical simulation has a certain accuracy. ③ When the inlet displacement is 30 L/s and the speed is 1400 r/min, the maximum value of the numerical solution of the output torque of a single rotor group is 12.45 N/m. When the inlet displacement increases from 18 L/s to 30 L/s, the maximum torque numerical solution increases from 10.78 N/m to 27.44 N/m.

Keywords: turbodrill; rotor; numerical simulation; output characteristics

check for updates

Academic Editor: Davide Lengani

Received: 3 January 2025
Revised: 27 January 2025
Accepted: 6 February 2025
Published: 8 February 2025

Citation: Li, W.; Chen, F.; Cao, M.; Ma, T.; Ning, W.; Zhang, M.; He, T.; Wang, X. Comprehensive Analysis of the Output Characteristics of Flow Field in Turbodrill Motor. *Machines* **2025**, *13*, 127. https://doi.org/10.3390/machines13020127

Copyright: © 2025 by the authors. Licensee MDPI, Basel, Switzerland. This article is an open access article distributed under the terms and conditions of the Creative Commons Attribution (CC BY) license (https://creativecommons.org/licenses/by/4.0/).

1. Introduction

With the increasing number of deep and ultra-deep wells, the bottleneck of drilling tools with low drilling speed has become increasingly obvious [1–3]. Drilling can be achieved using a variety of drilling tools, including positive displacement screw drills, blade-type turbodrills, and electric drills [4–6]. The screw drill has a lower rotation speed and smaller cutting force, and is inferior to the turbodrill in terms of drilling depth and drilling efficiency [7]. Turbine drilling technology is one of the effective methods for efficient drilling. Due to its high rotation speed and cutting force, the drilling task can be completed in a shorter time. Turbine drilling technology is mainly a downhole power motor, which is generally composed of main components such as a turbine section, support section, and reducer [8].

In the 1930s, Soviet engineer M. A. Kapelyushuikov first applied turbine technology to drilling, and turbine drilling technology has since become the basic method of oil drilling in the Soviet Union [9]. In addition, the combination of turbodrilling technology and other speed-reduction devices has increased the drilling speed and torque of turbodrills. In the

1970s and 1980s, Russia was the first to manufacture turbodrills with speed reducers, which were widely used in oil field drilling [10]. PDC drill bits have developed rapidly in Asia in recent years. In 2000, a new type of PDC drill bit developed and produced by China University of Petroleum (East China) began to be tested in the West Siberian oil fields in Russia, in combination with three types of reduction turbodrills [11].

In recent years, low-speed turbodrill drilling technology has made great progress, which has been reported by well-known turbodrill companies such as Neyrfor, VNIIBT-Drilling Tools, and Halliburton Sperry. Among the turbodrills developed by these drilling companies, their unique advantages, such as the ability to drill through hard and abrasive formations, have also attracted attention and attracted many scholars to conduct research [12,13]. At present, the research on low-speed, high-torque turbine drilling technology mainly focuses on the influence of blade structural parameters [14], the relationship between operating parameters and output performance and flow field characteristics, and the turbine stator and rotor structure [15]. On the other hand, appropriately optimizing the parameters of the turbine stator and rotor blades can effectively increase the torque of the turbodrill and improve the output efficiency of the turbodrill [16]. When the drilling fluid acts on the turbine stator and rotor, the kinetic energy of the fluid is mainly converted into the rotation of the turbine. As a result, the turbodrill has a high rotation speed during drilling, but the torque generated is too small to drill through hard rock. The high rotation speed problem can only be improved by increasing the length of the turbine section. Usually, the length of the turbine section is increased to about 100 stages [17]. However, an overly long turbine section is not conducive to downhole drilling [18]. Therefore, it is difficult to achieve high-torque turbodrills by increasing the length of the turbine section. Instead, high torque output is achieved by adding a reducer [19]. Some scholars have attempted to study the application of high-torque turbodrills in underground wells [20]. In order to improve the torque of turbodrill equipment, Ji Bo [21] proposed a new turbodrill device with a reducer superimposed on a turbine section structure. Yuan Xinmei [22] designed a turbodrill movable tooth reducer structure. Performance analysis showed that the device can significantly improve the torque output characteristics of the turbodrill. Xu Fudong et al. [23] proposed a new turbodrill reduction device and analyzed the turbodrill output characteristics through numerical simulation. These studies have played an important role in promoting the development of low-speed turbodrill restraints.

The feasibility and efficiency of low-speed turbodrill technology in the field of drilling have been gradually proven. Current research mainly focuses on optimizing the blade structure or adding a speed reducer to reduce the turbine speed and increase the torque. There are few reports on using low-speed, high-torque turbodrills to improve the rock-breaking effect of turbodrills, and there are mainly two problems. First, the structural design must not only meet the advantages of turbodrills with high drilling speed, but also keep the equipment use time moderate and the maintenance frequency efficient. Secondly, the stator and rotor structure and the reasonable arrangement of the flow channel in the low-speed and high-torque turbodrill must be ensured to improve the torque output performance of the turbodrill. Therefore, the reasonable design and systematic analysis of the stator and rotor structure and internal flow channel of the low-speed turbodrill is an important research direction to further improve the torque of the turbodrill.

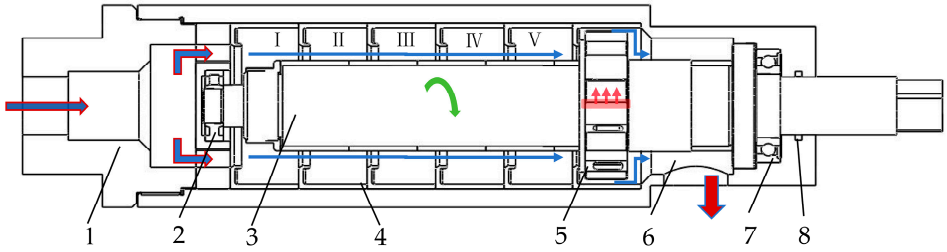
This paper takes into full consideration the complexity of the turbine stator and rotor rotation process and the difficulty of outputting large torque characteristics between the output shafts, and proposes an innovative motor structure based on the principle of turbine stator and rotor rotation form. Based on computational fluid dynamics (CFD), the commercial software Fluent is used to analyze the output characteristics of this rotor. The output characteristics of this new motor under different displacement continuous water

phase media conditions are verified by experiments, including parameters such as torque, speed, pressure drop, and power.

2. Technical Analysis

2.1. Structural Design

The internal structure of the test prototype is shown in Figure 1. It consists of an outer cylinder, an output shaft, a tapered roller bearing, a thrust bearing, a sleeve, a pump joint, a stator, and a rotor. The prototype is a cylindrical structure with a water phase inlet on the left and a tangential outlet on the right. To facilitate the measurement of the torque value generated by this type of rotor, the right-end output shaft is set to a square port. In order to offset the axial force generated by the water phase medium, a thrust bearing is installed on the left end.



1. pump connector 2. tapered roller bearings 3. output shaft 4. stator
5. rotor 6. outer cylinder 7. thrust bearing 8. sealing ring

Figure 1. Schematic diagram of the turbodrill test prototype.

2.2. Working Principle

Regarding the flow of uniform and continuous water phase medium from the left end of the inlet into the prototype, the form of the flow channel gradually transforms the axial movement of the fluid into a tangential jet movement, and then the fluid begins to flow through the stator–rotor formation of the cavity structure of the exchange of tangential and axial movement. Through the above form of fluid movement, at the same time, regarding the uniform density of drilling fluid under the action of the inlet high pressure to the next level of the new stator–rotor structure, the structure utilizes the principle of kinetic energy to move the liquid into the mechanical energy of the output shaft, so that the prototype output end of the shaft rotates and thus generates torque. The output shaft end produces different output characteristics at different fluid displacements.

3. Numerical Simulation

3.1. Fluid Domain Model Establishment

The main structure of the fluid domain is shown in Figure 2. The inner diameter length D_1 of the annular liquid inlet chamber is 80 mm, the liquid inlet chamber L_1 = 80 mm, the length of the rotor liquid guide channel is L_2 = 54 mm, the length of the outlet pipe is L_3 = 126 mm, the rotor cross-sectional diameter is D_2 = 137 mm, the diameter at the tail pipe is D_3 = 104 mm, the rotor slot length a = 6.5 mm, and the width b = 20 mm.

The simulation model of the rotor was established using Gambit 2.4.6 software. Due to the high quality of the fluid domain model, hexahedron and tetrahedron dual structure grids were used for meshing. The meshing model uses a segmented local refinement method to divide the inlet chamber, rotor flow channel, stator flow channel, and outlet cavity into different parts, refine the grid at the rotor injection port and the grid near the wall area, and improve the accuracy of numerical simulation.

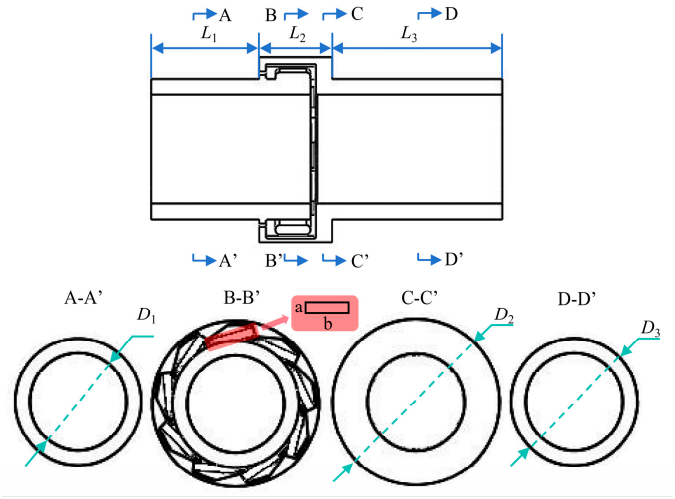


Figure 2. Rotor structure and main parameters.

By establishing rotor fluid domain models with different grid levels, grid independence tests are performed to eliminate the influence of the number of grids on the numerical simulation results. The results show that as the number of grids increases from 231,860 to 610,620, the torque generated by the analyzed curved rotor increases significantly. When the number of grids increases from 610,620 to 755,310, the rotor torque value changes slightly. Therefore, the numerical simulation uses a fluid domain model with a grid number of 610,620 to shorten the calculation time. The five grid division results of the rotor fluid domain model and the details of the selected structural grid are shown in Figure 3, and the independence test results are shown in Figure 4.

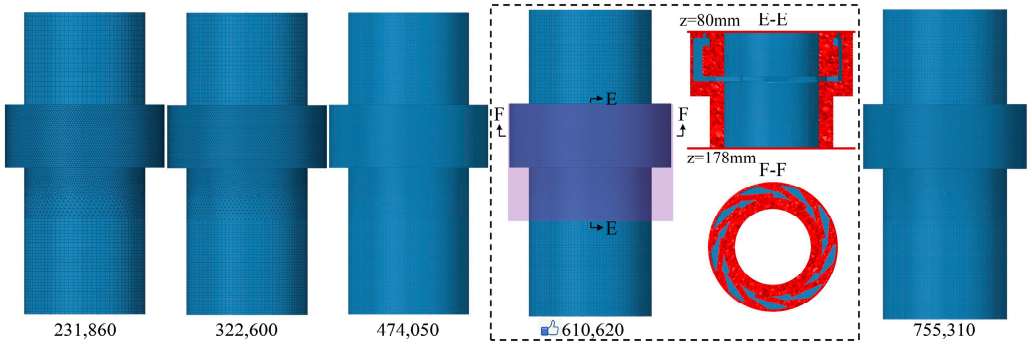


Figure 3. Five meshing results.

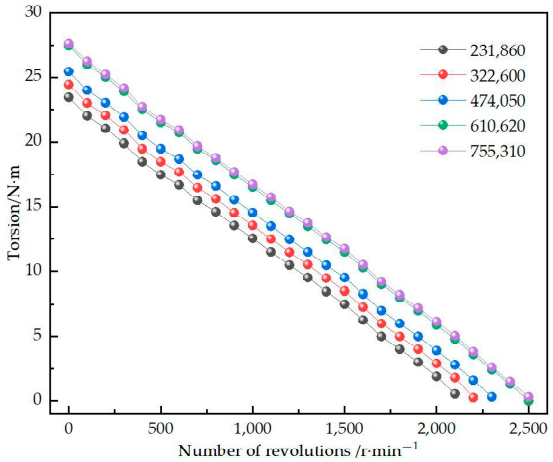


Figure 4. Grid independence test results.

3.2. Mathematical Model

3.2.1. Control Flow Model

The continuity equation of drilling fluid (water) is expressed as follows:

$$\frac{\partial}{\partial t}(\varphi_c \rho_c) + \nabla \cdot (\varphi_c \rho_c u_c) = 0 \tag{1}$$

where φ_c is the volume fraction of the drilling fluid (water), ρ_c is the density of the drilling fluid (water), and u_c is the velocity of the drilling fluid (water).

3.2.2. Basic Equations of Turbulence

The fluid velocity is much lower than the speed of sound, and its Mach number is much less than 1, which can be regarded as viscous incompressible flow. The continuity equation is

$$\partial \overline{u}_i / \partial x_j = 0 \tag{2}$$

The momentum equation (Reynolds time-averaged Navier–Stokes equation, also known as Reynolds equation) is

$$\frac{\partial(\rho \overline{u}_i)}{\partial t} + \frac{\partial}{\partial x_j}(\rho \overline{u}_i \overline{u}_j) = -\frac{\partial \overline{p}}{\partial x_i} + \frac{\partial}{\partial x_j}(\mu \frac{\partial \overline{u}_i}{\partial x_j} - \rho \overline{u_i' u_j'}) \tag{3}$$

where ρ is the density, and $\overline{u}_1$, $\overline{u}_2$, and $\overline{u}_3$ are the components of the velocity vector $\vec{u}$ in the x, y, and z directions (i, j = 1, 2, 3; $x_1 = x$; $x_2 = y$; $x_3 = z$). The pulsating motion equation is

$$u_i = \overline{u}_i + u_i' \tag{4}$$

Defined, $-\rho \overline{u_i' u_j'}$ is Reynolds stress; that is,

$$\tau_{ij} = -\rho \overline{u_i' u_j'} \tag{5}$$

Here, τ_{ij} actually corresponds to six different Reynolds stress terms, namely three normal stresses and three shear stresses.

3.2.3. Realizable *k*-*ε* Turbulence Model

The Standard *k*-*ε* turbulence model may lead to negative normal stress when the time-averaged strain rate is particularly large. In order to make the flow conform to the physical laws of turbulence, some mathematical constraints on the normal stress are required. To ensure the realization of this constraint, the coefficient C_μ in the turbulent viscosity calculation formula should not be a constant, but should be combined with the strain rate, thus proposing the Realizable *k*-*ε* model. In this model, the transport equations for k and ε are [24–26] as follows:

$$\frac{\partial}{\partial t}(\rho k) + \frac{\partial}{\partial x_i}(\rho k u_i) = \frac{\partial}{\partial x_j}[(\mu + \frac{\mu_t}{\sigma_k})\frac{\partial k}{\partial x_j}] + G_k - \rho\varepsilon \tag{6}$$

$$\frac{\partial}{\partial t}(\rho \varepsilon) + \frac{\partial}{\partial x_i}(\rho \varepsilon u_i) = \frac{\partial}{\partial x_j}[(\mu + \frac{\mu_t}{\sigma_\varepsilon})\frac{\partial \varepsilon}{\partial x_j}] + \rho C_1 E \varepsilon - \rho C_2 \frac{\varepsilon^2}{k + \sqrt{v\varepsilon}} \tag{7}$$

where $C_\mu = \frac{1}{A_0 + A_s U^* k/\varepsilon}$, $C_1 = \max(0.43, \frac{\eta}{\eta+5})$.

C_μ is no longer a constant. The parameters in the C_μ calculation formula are calculated according to the following formula:

$$A_0 = 4.0, A_s = \sqrt{6}\cos\phi,\ \phi = \tfrac{1}{3}\arccos(\sqrt{6}W),\ W = E_{ij}E_{jk}E_{ki}/(E_{ij}E_{ij})^{1/2},$$
$$U^* = \sqrt{E_{ij}E_{ij} + \Omega_{ij}\Omega_{ij}},\ \Omega_{ij} = \Omega_{ij} - 2\varepsilon_{ijk}\omega_k,\ \Omega_{ij} = \overline{\Omega}_{ij} - \varepsilon_{ijk}\omega_k$$

Here $\overline{\Omega}_{ij}$ is the time-averaged rotation rate tensor observed from a reference frame with angular velocity ω_k, which is specifically used to represent the effect of rotation. The specific meaning and value of each parameter can be found in reference [24].

Compared with the Standard *k*-ε model, the main changes of the Realizable *k*-ε turbulence model are as follows: the calculation formula of the turbulent viscosity has changed, C_μ is no longer a constant, but the content related to rotation and curvature has been introduced. The second to last term in the ε equation does not have any singularity; even if the *k* value is very small or 0, there is no problem of the denominator being 0, which is very different from the Standard *k*-ε model and the RNG *k*-ε model.

The Realizable *k*-ε model has been effectively used for various types of flow simulations, including rotating uniform shear flow, free flow (including jets and mixing flows), flow in pipes, boundary layer flows, and flows with separation.

3.2.4. Wall Function Method

Both the Standard *k*-ε turbulence model and the RNG *k*-ε turbulence model are established for turbulent flows with fully developed turbulence, and are turbulence calculation models suitable for high Reynolds numbers. For the flow in the near-wall region, the Reynolds number is low, the turbulence is not fully developed, and the pulsation effect of turbulence is not as great as the effect of molecular viscosity. Especially in the viscous bottom layer, the flow is almost laminar, and turbulent stress has almost no effect. The *k*-ε model established earlier cannot be used to solve the flow in this region.

The wall function method is a set of semi-empirical formulas. The basic idea is to use the *k*-ε model to solve the flow in the turbulent core area, but not to solve it in the wall area. The semi-empirical formula is used to directly link the physical quantities on the wall with the solution variables in the turbulent core area. In this way, the node variable values of the control volume adjacent to the wall can be directly obtained without solving the flow in the wall area.

The wall function method can be combined with the *k*-ε model to solve flow calculation problems near the wall and under low Reynolds number conditions.

3.2.5. Sliding Mesh Model

As shown in Figure 5, the sliding mesh technology for fixed-axis rotation is divided into several regions when the geometric model is meshed. The sliding mesh technology allows the meshes on both sides of the interface to slide against each other, without requiring the mesh points on both sides of the interface to coincide with each other. However, the flux on both sides of the interface must be calculated and made equal. The interface between the regions is the link between the regions, and data are transmitted through it [27–30]. When calculating the sliding mesh, the mesh does not need to be reconstructed, and the model used for the calculation is the normal control equation. After each time step iteration, the entire sliding area moves in a specified manner, and then the next time step iteration calculation is performed.

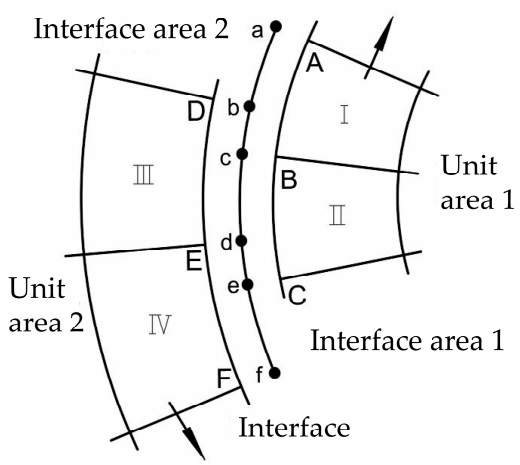


Figure 5. Theory of sliding grid.

Based on the Realizable *k*-ε turbulence model and sliding grid model introduced above, combined with the wall function method, the CFD analysis of the internal flow field of the jet rotor was carried out using Fluent software, and the output performance parameters of the drilling tool were obtained by calculation.

3.3. Boundary Conditions

In this study, the ANSYS-Fluent 19.0 solver was used to predict the output performance parameters (including torque, pressure drop, speed, and efficiency) of the motor. Among the existing turbulence models, the *k*-ε turbulence model was used to simulate the flow in the motor. Experimental water (water phase medium density is 1000 kg/m^3) is selected as the drilling fluid, and its density is equivalent to half of the actual drilling fluid density. The viscosity of the water phase medium is 1.003 mPa·s, and the physical parameters of the water phase are consistent with the results of the numerical simulation test. The inlet boundary condition is velocity inlet, the inlet displacement is in the range of 14 L/s~30 L/s, the outlet boundary condition is pressure outflow, and the flow weight is 1. The double-precision pressure algorithm is used to solve the steady-state solution. The COUPLE algorithm is used for velocity–pressure coupling, and the pressure coupling uses the pressure staggered option (PRESTO). The momentum, turbulent kinetic energy, and turbulent dissipation rate are second-order upwind schemes, and the convergence accuracy is set to 10^{-6}. Anti-slip conditions and impermeable conditions are set on the wall, and the wall function method is used to calculate the near-wall shear stress, turbulent kinetic energy, and turbulent dissipation.

4. Test Methods

The whole of the test prototype, namely the outer cylinder, stator, rotor, center shaft, and other parts, are made of 45# steel to provide conditions for high-pressure experiments. Its output performance was evaluated through the test process. Its main parts are shown in Figure 6. The test connection process is shown in Figure 7.

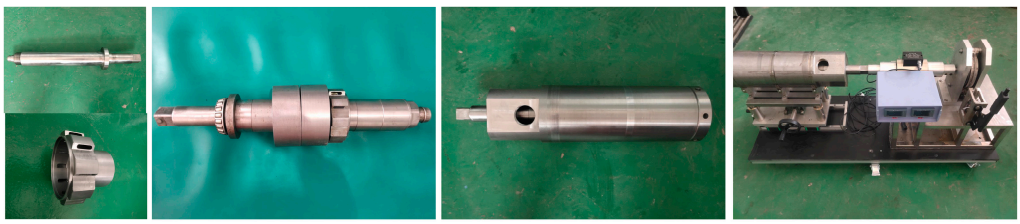
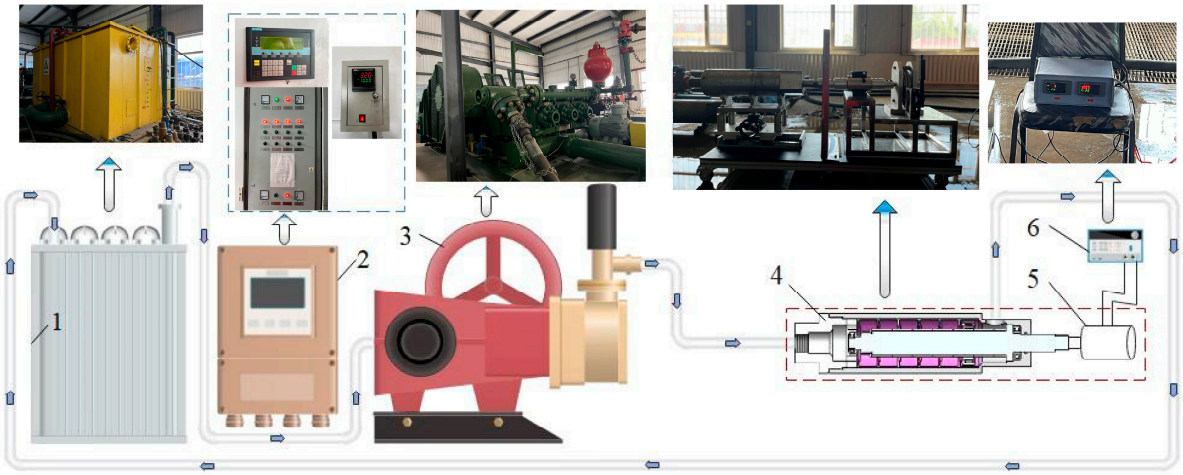


Figure 6. Main components of the test prototype.



1. water tank 2. piston pump control terminal 3. triplex piston pump
4. test prototype 5. torque sensors 6. torque tachometer

Figure 7. Test process diagram.

The HCNJ-101 series dynamic torque sensor (Beijing Haibohua Technology Co., Ltd., Langfang, China), with a maximum speed of 6000 r/min and a maximum torque of 1000 N·m, is used to obtain the speed and torque values of the motor in the test prototype. The supporting equipment HN-201 torque tachometer (Beijing Haibohua Technology Co., Ltd., Langfang, China) (dual display instrument) is used to directly display the torque and speed values, as shown in Figure 8.

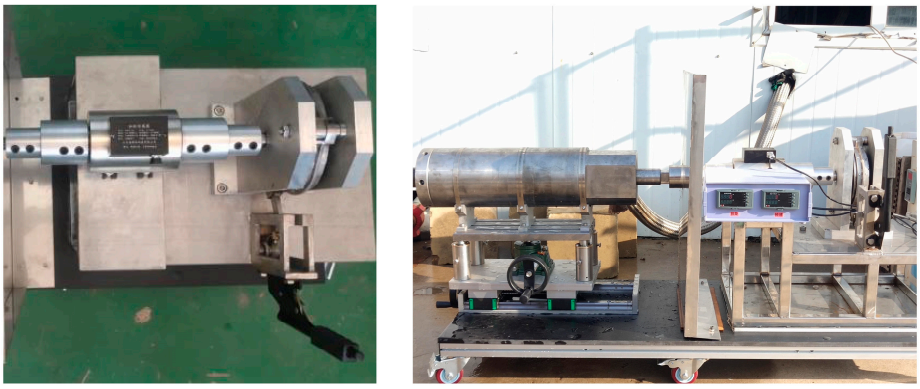


Figure 8. Torque sensor and torque tachometer.

Function: standard reset; torque and speed: two-way 4–20 mA transmission, and RS485 communication. The drilling fluid (water phase medium) is stored in the water tank, and the water phase medium is transported by a three-cylinder plunger pump. The displacement of the plunger pump is adjusted by the controller, and the throttling control valve is connected to the rear to control the flow entering the device. The temperature in the water tank can be adjusted to ensure a constant value; here the water temperature is 25 °C. A certain flow of drilling fluid enters the test sample. The output shaft end of the device is connected to the dynamic torque sensor through a coupling. The liquid flowing through the test sample is collected again in the water tank. The pressure values at the inlet and outlet pipes are obtained through the pressure drop digital display.

5. Results and Discussion

5.1. Single Motor Output Characteristics

In order to obtain the output response characteristics of a single motor in the test prototype under a certain displacement of drilling fluid, a numerical simulation was carried out on the above model to simulate the motor output of a single motor under displacement Q = 30 L/s and different speeds, and the important output parameter values were plotted into a curve, as shown in Figure 9.

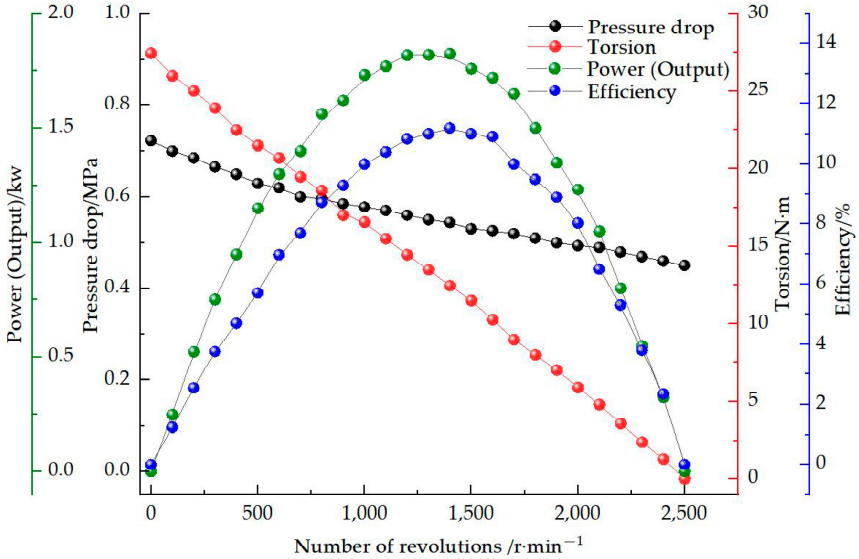


Figure 9. Motor output performance curve.

It is not difficult to see from the figure that when the motor speed changes from 0 r·min^{-1} (braking state) to rotation, its output power and efficiency both show a gradually increasing trend with the increase in speed; when the speed reaches 1400 r·min^{-1}, the power value and efficiency value reach the peak value of 1.83 kw and 11.20%, respectively. When the speed continues to increase to 2500 r·min^{-1}, the power value and efficiency gradually decrease from the peak value to 0. The pressure drop and torque output values decrease with increasing speed. When the speed is 0 (that is, the turbine does not start to rotate), the hydraulic power of the drilling fluid is fully converted into torque output. At this time, the turbine output torque value is the maximum value of 27.44 N·m. Since there is no rotation output, the pressure drop value reaches a maximum of 0.72 MPa. When the turbine reaches the maximum speed, the turbine is in an idling state, its torque value is 0, and the pressure drop value is a minimum of 0.45 MPa. From the data values presented in the figure, it can be concluded that the output characteristics of the turbine motor are similar to the output characteristic curve of the existing axial flow turbodrill motor structure [31], and it has a larger torque output value than the existing axial flow motor turbodrill.

5.2. Torque Difference of a Single Motor with Different Displacements

In order to further analyze the torque output characteristics of the motor under different displacements, further numerical simulation analysis and experimental verification are carried out on the above structure. The numerical simulation results and the experimental results are plotted and compared, and the results are shown in Figure 10.

It is not difficult to infer from the figure that, whether it is a numerical simulation or experiment, the peak torque value of the motor shows an increasing trend with the increase in flow rate, and under the same flow rate, the torque value shows a decreasing trend with the increase in speed. Since the torque value of motors with the same structure has

the same decreasing trend when the drilling fluid displacement increases from 18 L/s to 30 L/s, the drilling fluid flow rate Q = 24 L/s is taken as an example for analysis. When the speed is 0 r·min^{-1}, the maximum torque value of the simulation value is 19.19 N·m, and the test value is 18.19 N·m, with a relative change rate of 5.21%. As the speed increases, the torque value of the motor gradually decreases. When the speed reaches 2000 r·min^{-1}, the simulated torque value decreases to 0.27 N·m, which is close to 0. The test value shows that when the torque value of the rotor is 0, its speed is close to 1800 r·min^{-1}, and the relative change rate is approximately 10%. The reason is that in the actual test, the viscosity of the water, the smoothness of the pipeline, and the power loss of the plunger pump itself will lead to the overall energy consumption in the device, and the simulation process excludes a series of resistance factors, resulting in a larger calculated value. However, overall, the test curve and the simulation curve show good consistency, indicating that the simulation value can provide certain support for the test data, and it is believed that the simulation has a high degree of credibility.

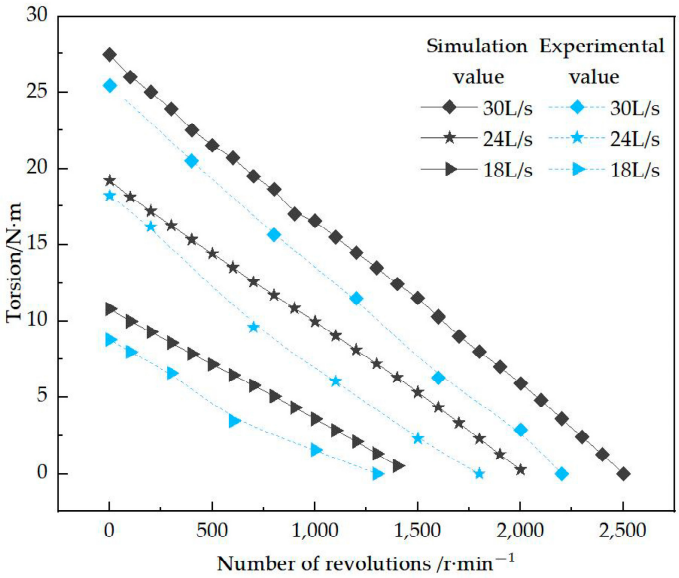


Figure 10. Motor torque changes with speed under different displacements.

5.3. Velocity Field Distribution in a Single Motor Group

In order to obtain the flow velocity change in the fluid more clearly, the numerical simulation results of the motor under three displacements of 18 L/s, 24 L/s, and 30 L/s were selected, and the flow field distribution in the motor and the changes in the output characteristic parameters were analyzed. The velocity distribution cloud diagrams under the three displacements are shown in Figure 11.

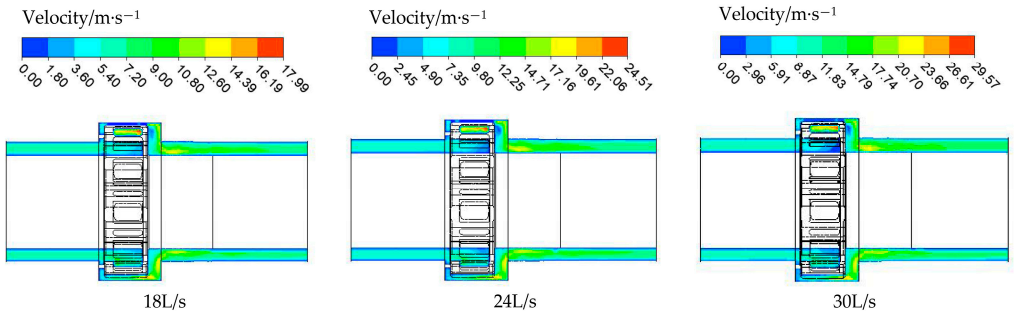


Figure 11. Cloud diagram of flow velocity variation in the motor under different displacements.

It can be clearly seen from the figure that the velocity changes when the drilling fluid passes through the motor flow channel. The velocity value gradually increases from the inlet to the rotor jet port, and the velocity value decreases significantly from the jet outlet to the rotor tail position. To further illustrate the cloud map, five data points at the same position were selected for the three working conditions and plotted into curves, as shown in Figure 12.

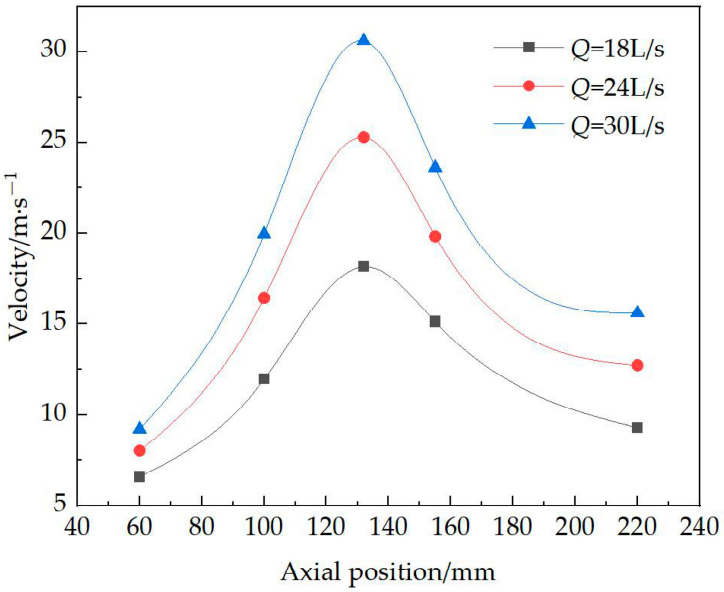


Figure 12. Motor speed versus axial position curves at different displacements.

It can be concluded from the figure that when the motor is rotating, the flow rate of the liquid inside it increases with the increase in displacement, and the flow rate of the internal fluid also shows the same trend at different positions with the same displacement; so Q = 18 L/s is taken for explanation. When the axial distance is 60 mm, the drilling fluid has just entered the flow channel, and the drilling fluid velocity is the lowest at 6.59 m/s. As time goes by, the drilling fluid velocity gradually increases. When the axial distance from the inlet is 132 mm, the drilling fluid velocity reaches a maximum value of 18.18 m/s, and at the cross-sectional position of 220 mm, the drilling fluid velocity decreases to 9.31 m/s. The reason is that the drilling fluid has a certain pressure and kinetic energy during the flow process. When the drilling fluid flows through the motor, the flow path of the fluid gradually decreases and the direction changes, giving the fluid the ability to jet. Therefore, the flow rate of the fluid increases after passing through the motor. After the fluid converts the kinetic energy into the mechanical energy of the motor, the speed of the fluid decreases again, which shows a trend of decreasing drilling fluid flow rate.

5.4. Pressure Field Distribution Inside a Single Motor

In order to more accurately analyze the change of flow field pressure in the motor under the same drilling fluid displacement condition, the numerical simulation and test results of the motor with a drilling fluid displacement of 18 L/s~30 L/s were selected. Through numerical simulation and tests, the data curve of the flow field pressure drop in the motor when the drilling fluid displacement changes is shown in Figure 13.

The figure above shows that the pressure drop inside the motor is inversely proportional to the motor's own speed within a certain range. The reason for this is that as the motor speed increases, the pressure loss of kinetic energy converted into mechanical energy gradually decreases; at the same time, as the displacement continues to increase,

the amplitude of the pressure drop increases, and the motor speed range is expanded, indicating that the drilling fluid displacement has a certain effect on the motor's mechanical energy output. The larger the displacement, the greater the energy of the drilling fluid converted into mechanical energy, and the motor speed will also increase accordingly.

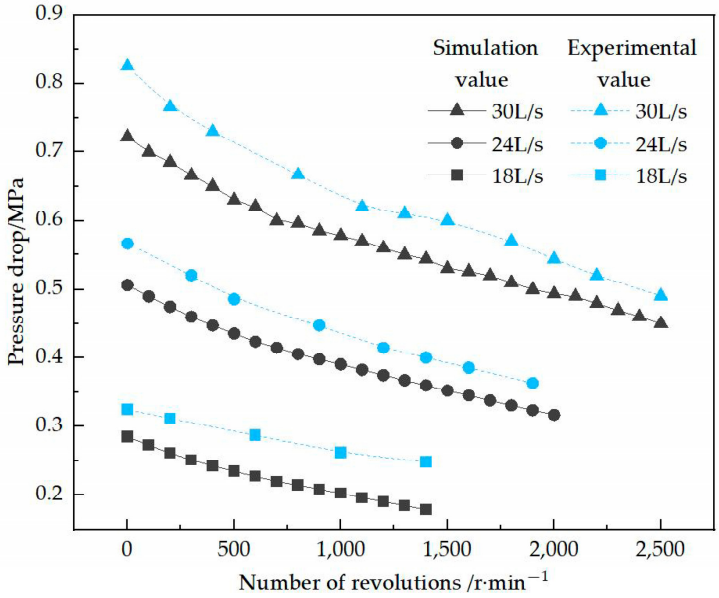


Figure 13. Motor pressure drop curve with speed under different displacement.

When the motor speed is 800 r·min^{-1}, the displacement of different drilling fluids is 18 L/s, 24 L/s, and 30 L/s, and numerical simulation analysis is performed. The cloud map results are shown in Figure 14.

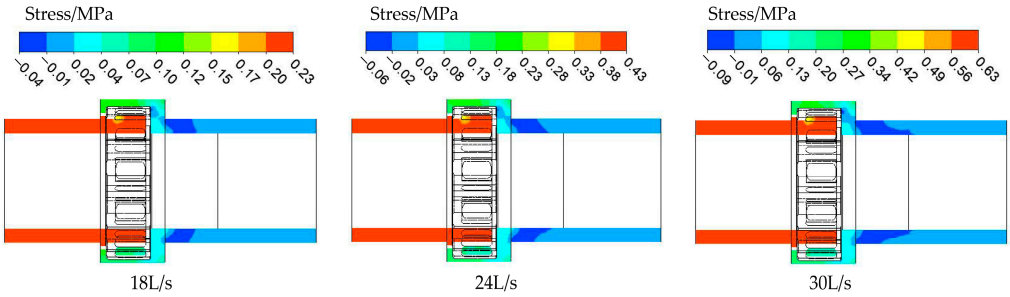


Figure 14. Cloud diagram of pressure change in the flow field of the motor under different displacements.

It is not difficult to see from the figure that the pressure changes in the three cases are relatively similar (all gradually decrease from left to right), so the drilling fluid displacement is taken as 24 L/s for illustration. Before the drilling fluid enters the motor, the pressure value is relatively large, which is 0.43 MPa. As the drilling fluid enters and flows out of the motor, the drilling fluid pressure decreases sharply to 0, indicating that the drilling fluid pressure potential energy is converted into motor kinetic energy with a relatively good effect and a high energy conversion efficiency.

6. Conclusions

Under the same displacement, speed, and operating conditions, numerical simulation and torque speed output performance tests were carried out on the new motor in the test prototype. The velocity field and pressure field distribution and output characteristic

parameters of the motor in the prototype were systematically analyzed, and the following conclusions were drawn:

(1) The blades of traditional turbodrills are mostly axial flow, the kinetic energy of the liquid converted into the torque energy of a single set of turbine stators and rotors is small, and the overall output speed of the turbine is relatively high. By improving the structure of the turbine blades and creating a liquid axial flow channel to convert the jet channel, the structural form is used to change the flow direction of the liquid acting on the rotor structure, causing it to jet, thereby increasing its output torque and reducing the output speed. This overcomes the defect of high speed and low torque output of conventional turbines and effectively ensures the compatibility of the drill bit with them.

(2) The numerical simulation method was used to verify that the output characteristics of the new turbine are the same as those of the conventional turbine, and that the relationship between the output parameters of pressure drop, torque, power, and efficiency of a single turbine and the speed is obtained by using the calculation point method.

(3) The model and method used in numerical simulation are briefly introduced in the form of theoretical derivation. The numerical simulation method was used to calculate that when the drilling fluid displacement is 18 L/s, 24 L/s, and 30 L/s, the pressure drop and torque of the turbine with new structural form within the research scope show a downward trend when its speed increases, and when its displacement increases, the maximum torque value and the maximum pressure drop value show an upward trend. At the same time, the numerical simulation calculation results were compared and verified by indoor tests, and the relative error between the test value and the numerical simulation value was calculated to be within 10%.

(4) When the displacement is 30 L/s, the velocity of the longitudinal section of the flow field in the motor increases first and then decreases with the increase in the axial position, and the maximum velocity in the flow field is 30.6 m/s.

(5) The successful verification and analysis of indoor tests show that the newly developed turbine structure can make up for the fact that conventional turbines need to be equipped with a reducer device to achieve the performance of reducing speed and increasing torque, providing data support for the widespread promotion of this new turbine structure.

Author Contributions: Conceptualization, W.L. and F.C.; Methodology, M.C.; Software, M.Z. and W.N.; Formal analysis, T.M. and T.H.; Resources, F.C. and X.W.; Writing—original draft, F.C.; Supervision, M.C.; Project administration, W.L.; Funding acquisition, W.L. and F.C. All authors have read and agreed to the published version of the manuscript.

Funding: This work was supported by the National Natural Science Foundation of China under contract No. 52274005.

Data Availability Statement: The raw data supporting the conclusions of this article will be made available by the authors upon request.

Conflicts of Interest: The author Wei Li is employed by Northeast Petroleum University. The remaining authors declare that the research was conducted in the absence of any commercial or financial relationships that could be construed as potential conflicts of interest.

References

1. Sun, L.D.; Zou, C.N.; Zhu, R.K.; Zhang, Y.H.; Zhang, S.C.; Zhang, B.M.; Zhu, G.Y.; Gao, Z.Y. Formation, distribution and potential of deep hydrocarbon resources in China. *Petrol. Explor. Dev.* **2013**, *40*, 641–649. (In Chinese) [CrossRef]

2. Zheng, R.Q.; Zhao, Y.; Wang, W.; Hou, S.; Li, B.; Liu, C.P. Optimization design of hydraulic rotary punching tool and turbodrill. *West-China Explor. Eng.* **2020**, *32*, 31–34. (In Chinese)
3. Jia, C.Z.; Pang, X.Q.; Jiang, F.J. Research status and development directions of hydrocarbon resources in China. *Pet. Sci. Bull.* **2016**, *1*, 2–23. (In Chinese) [CrossRef]
4. Liu, L.; Wang, Y.; Wang, Z.Q.; Lu, J.X.; Zhang, K.; Liu, B.L. Research status and key technology of meta-to-metal screw PDM drills. *Explor. Eng. (Rock Soil Drill. Tunneling)* **2020**, *47*, 24–30. (In Chinese)
5. Guan, F.; Wan, F.; Wu, Y.S.; Zhang, Q. Research status of turbodrill. *CPM* **2021**, *49*, 1–7. (In Chinese)
6. Li, X.Y.; Han, F.; Wang, A.G. Current status and prospects of electric drilling tools drilling technology. *China Pet. Chem. Stand. Qual.* **2021**, *41*, 169–171. (In Chinese)
7. Ren, J. Analysis on the development and technical advantages of russian. *Technol. Dev. Enterp.* **2013**, *32*, 73–74. (In Chinese)
8. Tyraspolsky, W. *Downhole Hydraulic Drilling Tool*; Petroleum Industry Press: Beijing, China, 1991.
9. Kapelevich, A.L. Geometry and design of involute spur gears with asymmetric teeth. *Mech. Mach. Theory* **2000**, *35*, 117–130. [CrossRef]
10. Zhao, N.; Cai, J.L.; Pan, H.Z. A new type of turbodrill with gear reducer. *CPM* **2000**, *28*, 51–52+56. (In Chinese) [CrossRef]
11. Chen, H.B.; Zhou, L.C.; Zhang, L.; Yang, S.J. Successful applications of turbine tool driven PDC bits with reducers in the West Siberia Oilfields. *Pet. Drill. Tech.* **2005**, *33*, 48–50. (In Chinese)
12. Feng, D.; Liu, T.L.; Wang, J.G.; Zhang, H. Advances in Foreign Turbodrill Technology. *CPM* **2020**, *48*, 1–9. (In Chinese) [CrossRef]
13. Zhao, L.D.; Li, L.X.; Wang, Y.; Xue, Q.L.; Liu, B.L. Summary of research progress in turbodrill. *Explor. Eng. (Rock Soil Drill. Tunneling)* **2016**, *43*, 267–274. (In Chinese)
14. Zhang, Y.H.; Zhang, Q.; Xin, Y.A.; Duan, C.W.; Ji, C.G. Modeling design and research of three-dimensional blades of 54mm turbodrill. *CPM* **2023**, *51*, 61–67. (In Chinese) [CrossRef]
15. Sha, J.J. Research on the Influence of Drilling Fluid Characteristics on the Output Performance of Turbodrills. Master's Thesis, China University of Geosciences, Beijing, China, 2020. [CrossRef]
16. Liu, Q. Optimized Design of Stator-Rotor Structure Parameters of Φ254mm Turbine Drilling Tool. Master's Thesis, China University of Petroleum, Beijing, China, 2021. [CrossRef]
17. Guo, B.S. Design & optimization of Φ73 mm diameter slimhole turbodrill stator & rotor's blade profile. *Oil Field Equip.* **2021**, *50*, 31–40. (In Chinese) [CrossRef]
18. Li, B. TRM reducing turbine drilling tools. *West-China Explor. Eng.* **2013**, *25*, 41–42+45. (In Chinese)
19. Zhang, X. Design and Optimization of Small-Diameter Turbodrill Reducer. Master's Thesis, China University of Geosciences, Beijing, China, 2021. [CrossRef]
20. Hu, Z.M. Principle and application of low speed and high torque turbodrill. *Oil Field Equip.* **1976**, 45–52. (In Chinese)
21. Ji, B. Development and application of turbodrill superimposed planetary reducer. *West-China Explor. Eng.* **2019**, *31*, 89–90+92. (In Chinese)
22. Yuan, X.M. Study on the Characteristics of the Oscillating Teeth Gear Reducer for the Turbine Drill Tool. Ph.D. Thesis, Yangtze University, Hubei, China, 2017.
23. Xu, F.D.; Fu, D.L. Transient pattern of dynamic performance of turbodrill with decelerator and simulation. *CPM* **1997**, *25*, 36–39. (In Chinese) [CrossRef]
24. Wang, F.J. *Computational Fluid Dynamics Analysis*, 1st ed.; Tsinghua University Press: Beijing, China, 2004; pp. 113–1322.
25. Fluent Inc. *Fluent User's Guide*; Fluent Inc: New York, NY, USA, 2023.
26. Yakhot, V.; Orzag, S.A. Renormalizaton group analysis of turbulence: Basic Theory. *J. Sci. Comput* **1986**, *1*, 3–51. [CrossRef]
27. Montante, G.; Lee, K.C.; Brucato, A.; Yianneskis, M. Numerical simulations of the dependency of flow pattern on impeller clearance in stirred vessels. *Chem. Eng. Sci.* **2001**, *56*, 3751–3770. [CrossRef]
28. Xu, Z.H.; Wu, Y.L.; Chen, N.X.; Liu, Y.; Zhang, L.; Wu, Y.Z. Simulation of turbulent flow in pump based on sliding mesh and RNG k-ε model. *J. Eng. Thermophys.* **2005**, *26*, 66–68. (In Chinese)
29. Jiang, F.; Chen, W.; Mai, M.; Li, Y.Y. Numerical simulation on water and sediments two-phase flows in river. *Prog. Saf. Sci. Technol. V* **2005**, *11*, 1634–1639.
30. Kris, R.; Jan, V.; Erik, D. An arbitrary Lagrangian-Eulerian finite-volume method for the simulation of rotary displacement pump flow. *Appl. Numer. Math.* **2000**, *32*, 419–433. [CrossRef]
31. Wang, J.L.; Bian, P.M.; Tao, X.H.; Lu, B.P.; Li, M.B. Development and application of an ultra short high energy turbodrill. *Explor. Eng. (Rock Soil Drill. Tunneling)* **2020**, *47*, 16–22. (In Chinese)

Disclaimer/Publisher's Note: The statements, opinions and data contained in all publications are solely those of the individual author(s) and contributor(s) and not of MDPI and/or the editor(s). MDPI and/or the editor(s) disclaim responsibility for any injury to people or property resulting from any ideas, methods, instructions or products referred to in the content.